Observation-based estimate of Earth's effective radiative forcing

Senne Van Loon*, Maria Rugenstein, and Elizabeth A. Barnes

Department of Atmospheric Science, Colorado State University, Fort Collins, Colorado, USA

This manuscript has been published in Proceedings of the National Academy of Science:

S. Van Loon, M. Rugenstein, & E.A. Barnes, Observation-based estimate of Earth's effective radiative forcing, Proc. Natl. Acad. Sci. U.S.A. 122 (24) e2425445122, https://doi.org/10.1073/pnas.2425445122 (2025).

*Corresponding author: Senne Van Loon; 970-491-8682; senne.van_loon@colostate.edu;
Colorado State University, Department of Atmospheric Science,
200 West Lake Street, 1371 Campus Delivery, Fort Collins, CO 80523-1371

The authors have no competing interests to declare.

Classification: Physical Sciences; Earth, Atmospheric, and Planetary Sciences

Keywords: Radiative forcing, Energy budget, Climate

Human emissions continue to influence Earth's climate. Effective radiative forcing quantifies the effect of such anthropogenic emissions together with natural factors on Earth's energy balance (Soden et al. 2018; Gregory et al. 2020; Forster et al. 2021, 2024). Evaluating the exact rate of effective radiative forcing is challenging, because it can not be directly observed. Therefore, estimating the effective forcing usually relies on climate models (Forster et al. 2024). Here, we present an estimate of effective radiative forcing that makes optimal use of observations. We use machine learning to learn the relationship between surface temperature and radiation caused by internal variability in a multi-model ensemble. Combining this with observations of surface temperature and the Earth's net radiative imbalance (Loeb et al. 2018, 2021; NASA/LARC/SD/ASDC 2023), we predict an effective forcing trend of $0.71 \pm 0.21\,\mathrm{Wm}^{-2}$ per decade for 2001-2024. This is a new and independent assessment of the observed effective radiative forcing since 1985, that can be updated simultaneously with available observations and aligns with our physical understanding of radiative feedbacks. We make advances to close the Earth's energy budget on annual timescales, by separating the influence of forcing versus the radiative response to surface temperature variations. Effective radiative forcing has substantially increased since 2021 and has not been countered by a strongly negative radiative response until 2024, consistent with exceptional warmth in 2023 and 2024.

Significance Statement: Effective radiative forcing is the radiative perturbation of the atmosphere before surface temperature changes. Quantifying this effect is key to understanding Earth's energy balance, testing climate theories, building climate models, and attributing climate change. Effective forcing cannot be observed and its calculation relies on climate models, which come with biases and assumptions of the radiative effect of emissions and cloud processes that are not understood well yet. Here, we develop a new framework to calculate historical forcing that makes minimal use of climate models, by combining artificial intelligence with direct observations. Our forcing estimate indicates a strong upwards trend in the last two decades, can be updated immediately with new observations, and increases our understanding of Earth's recent energy imbalance.

At the top of the atmosphere, effective radiative forcing (F) and the radiative response to surface warming (R) simultaneously modify the radiation budget of the Earth (N). The simplest energy balance model states that, globally averaged,

$$N = F + R. \tag{1}$$

Only N can be measured by satellites recording the energy flux in and out of the entire Earth system (Loeb et al. 2018, 2021; NASA/LARC/SD/ASDC 2023). A positive effective radiative forcing F (excess energy introduced into the atmosphere) is generally balanced by a negative response R, but both are time-varying. In a stable climate, R balances F. A positive N indicates excess energy storage in the Earth system.

Effective radiative forcing (hereafter "forcing" F) is the sum of instantaneous radiative forcing (initial flux changes after a perturbation in emissions or prescribed concentrations such as greenhouse gases or aerosols) and radiative adjustments (radiative flux changes induced by the forcing within the atmosphere but independent of surface temperature; e.g., Sherwood et al. 2015; Smith et al. 2020; Forster et al. 2021; Sherwood et al. 2020). Instantaneous radiative forcing has recently been estimated from observations using radiative kernels (Kramer et al. 2021), but radiative adjustments have to be added to make its use valid in equation (1) and to compare it to other estimates of radiative forcing (see discussion below; Forster et al. 2024). Radiative adjustments rely on climate models and are very uncertain. Here, we directly estimate effective radiative forcing without relying on the concept of radiative adjustments or climate models calculating them. Note that in Eq. (1), we define R to include only the temperature-driven feedbacks, while forcing adjustments are included in F.

Estimates of historical forcing are uncertain because it requires the input of external factors such as greenhouse gas concentrations or aerosol emissions and relies on specific implementations of parametrizations that can lead to model biases (Soden et al. 2018; Bellouin et al. 2020; Forster et al. 2021, 2024). Here, we present a new method to quantify effective radiative forcing from the observed surface temperature and radiative imbalance, using a minimal number of assumptions. We combine observations with physically explainable machine learning methods to predict the radiative response to surface warming, from which we subsequently estimate the historical radiative forcing.

1. Convolutional neural network predicts radiative response

The radiative response to surface warming R is an aggregate of many processes initiated by the perturbation of a forcing. For example, CO_2 or aerosols change the structure of temperature in the atmosphere and at the surface, and the amount and distribution of water vapour, clouds, snow, sea ice, and vegetation. In turn, all of these factors can change the radiation balance of the Earth, both in the net shortwave solar radiation and the longwave outgoing radiation (Charney et al. 1979; Cess et al. 1990; Roe 2009). Research over the last decade has highlighted that global-mean radiation sensitively depends on the spatial patterns of surface warming, termed the pattern effect (Senior and Mitchell 2000; Andrews et al. 2015; Rugenstein et al. 2023b).

We predict R from maps of surface temperature (T) with a convolutional neural network (CNN; Supporting Information Fig. 1 and Methods). CNNs have recently gained popularity in the geosciences (Reichstein et al. 2019), because they are well-equipped to recognize nonlinear spatial patterns in images (LeCun et al. 2015). It has been shown that CNNs outperform traditional and regularized linear methods in predicting global-mean radiative response to spatial variations of T caused by internal variability (Rugenstein et al. 2025). Here, we train a CNN to recognize the relationship between maps of T and the globally averaged R caused by internal variability in large initial condition ensembles of four climate models (see Methods). That is, the forced response is removed from all data prior to training by subtracting the ensemble mean, leaving only natural variations in T and R.

Training on internal variability removes the need to rely on the correct simulation of forcing or forced surface warming in climate models. We only make the assumption that climate models correctly simulate the relationship between the spatial pattern of T and global-mean R in an unperturbed climate. We do not argue that any individual model is fully correct (Forster et al. 2021; Maher et al. 2023; Myers et al. 2021), but rely on the spread and diversity in the multi-model ensemble to be broad enough to lie *around* the true relationship between T and R (Olonscheck and Rugenstein 2024).

The CNN replaces the usual approximation that R is linearly dependent on global-mean temperature (Gregory et al. 2004; Sherwood et al. 2020), which is unable to explain large variations of radiation in the historical record (Andrews et al. 2015; Gregory et al. 2020; Rugenstein et al. 2023b). Instead, the CNN takes into account the spatial pattern effect, along with potential nonlin-

100 earities among T and R. The CNN successfully reproduces held-back testing members with high
101 skill (Supporting Information Fig. 3a-b). Moreover, CNNs trained on data from only three models
102 can effectively predict R in the fourth model, indicating that our CNN can make out-of-sample pre-
103 dictions. Importantly, the CNN skilfully predicts the forced response to temperature patterns that
104 have seen strong radiative forcing (Supporting Information Fig. 3c-d). That is, applying the CNN
105 to simulated temperature maps from a warming climate (as opposed to the internal variability the
106 CNN is trained on), we correctly predict a negative trend in R. This is evidence that the CNN is
107 transferable to real-world climate change.

108 2. Quantifying observed radiative forcing

109 We estimate the historical forcing with Eq. (1) by quantifying R with our CNN, and subtracting
110 R from the observed N:

111 First, we apply observed surface temperature anomalies with respect to the 2001-2020 climatol-
112 ogy since 1985 to the CNN (Fig. 1, bottom blue lines). Different observational products result in
113 very similar radiation responses (see Methods). Crucially, these observation-derived temperature
114 maps have not been used to train the CNN, and they include a forced trend. Although the CNN
115 has not been trained on forced climate change, the predicted R has a significant negative trend, as
116 it should in a changing climate in which F increases (Raghuraman et al. 2021; Roe 2009; Knutti
117 and Rugenstein 2015).

124 Second, the radiative imbalance N can be derived from the satellite record (Fig. 1, middle black
125 line). Since 2001, these measurements are considered fairly precise (solid black line, derived from
126 CERES, Loeb et al. (2018)) but N has been reconstructed back to 1985 from older satellite products
127 (dashed black line, DEEP-C, Allan et al. (2014); Liu et al. (2020); Liu and Allan (2022)).

128 Finally, we quantify the forcing (Fig. 1, top red lines) by subtracting our predicted radiative
129 response from the observed imbalance (i.e., $F = N - R$). This new estimate of F primarily uses
130 observable quantities: the radiative imbalance and surface warming patterns. At the same time,
131 we limit the use of climate model input: the relationship between T and R learned from internal
132 variability only.

133 Our forcing estimate has a significant positive trend of $0.71 \pm 0.21\,\mathrm{Wm^{-2}decade^{-1}}$ (5%-95%
134 confidence range, see Methods) in the period 2001-2024 (Fig. 1, dotted red line). This con-

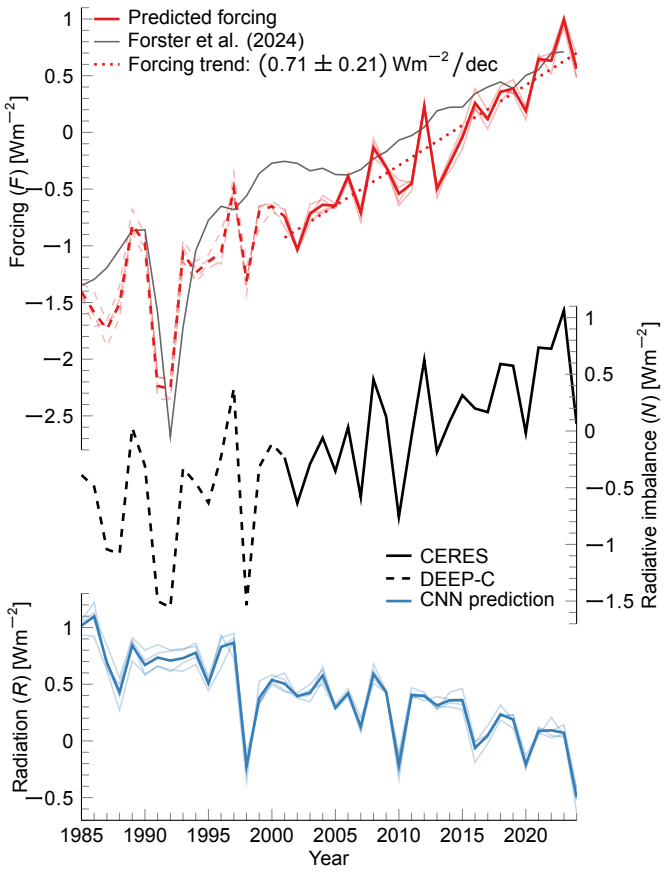

Fig. 1. **Radiative forcing derived from observations.** Bottom panel shows the radiative response to surface warming (R, blue) predicted by the convolutional neural network (CNN) from four observational surface temperature datasets (thin lines; thick line shows the average). Middle panel is the observed radiative imbalance (N, black). Top panel shows the predicted radiative forcing ($F = N - R$, red), and the dotted red line is the best linear fit for 2001-2024. As a comparison, the thin black line shows the radiative forcing from Forster et al. (2024). All R, N, and F values are anomalies with respect to the average of 2001-2020.

firms that the Earth system is experiencing a rapid increase in forcing. We predict a stronger trend in F than Forster et al. (2024) (top thin black line in Fig. 1), who predict a forcing trend in 2001-2023 of $0.51\,\mathrm{Wm^{-2}decade^{-1}}$ (5%-95% confidence range of $0.36\,\mathrm{Wm^{-2}decade^{-1}}$ to $0.68\,\mathrm{Wm^{-2}decade^{-1}}$, see methods). For the same period (2001-2023), we estimate a forcing trend of $0.72 \pm 0.20\,\mathrm{Wm^{-2}decade^{-1}}$.

Contrary to other methods, we can resolve interannual variability of the forcing. For example, we correctly predict a strongly negative forcing in 1991/1992, when natural aerosol emissions peaked

due to the 1991 Pinatubo eruption (Minnis et al. 1993; Stenchikov et al. 2009). Because we rely on observations of the radiative imbalance, which are limited to 1985-2024, we cannot estimate the forcing before 1985. Moreover, although the trend in the observed N is robust, satellite measurements alone are not accurate enough to detect the absolute value of the radiative imbalance (e.g., Loeb et al. 2021). Therefore, our estimates in Fig. 1 are defined with respect to the 2001-2020 climatology (see Methods). Thus, we do not constrain the absolute magnitude of the forcing compared to the pre-industrial era, but report on its trend and interannual variability with respect to the 2001-2020 average.

Andrews and Forster (2020) used a similar approach to constrain the magnitude of effective radiative forcing complementary to our current effort to derive the recent trends. They found $F = 2.3\,\mathrm{Wm}^{-2}$ ($1.7\,\mathrm{Wm}^{-2}$ to $3.0\,\mathrm{Wm}^{-2}$ confidence range, averaged over 2005-2015 with respect to the pre-industrial baseline 1861-1880) by calculating a global radiative feedback from atmospheric model simulations with observed sea surface temperature boundary conditions and combining it with N derived from in situ ocean observations (Johnson et al. 2016).

Over the last decade, the Earth energy imbalance has steadily increased (Hodnebrog et al. 2024; von Schuckmann et al. 2023; Storto and Yang 2024; Cheng et al. 2024) and may even be accelerating (Forster et al. 2024; Loeb et al. 2024b), most likely due to increased anthropogenic forcing (Raghuraman et al. 2021; Hodnebrog et al. 2024). Our results provide independent evidence that this increasing N is driven by an escalating F. Based on trend analysis, F increased by $0.51 \pm 0.61\,\mathrm{Wm}^{-2}$ from 2001 to 2010, and by $0.80 \pm 0.44\,\mathrm{Wm}^{-2}$ from 2011 to 2020, indicating an acceleration of the forcing. This acceleration could be explained by a reversed aerosol forcing trend (Quaas et al. 2022; Kramer et al. 2021), slowing down the global cooling effect of aerosols.

3. Validating our approach

Our method relies on the CNN to learn the correct relationship between R and surface temperature patterns. Although machine learning techniques are often regarded as a black box, explainable artificial intelligence (XAI) techniques (Mamalakis et al. 2022) allow us to understand why and how the CNN makes predictions.

Local gradients of the CNN explain the sensitivity of the CNN to local temperature variations and can be interpreted as radiative feedback arising from internal variability. Radiative feedback

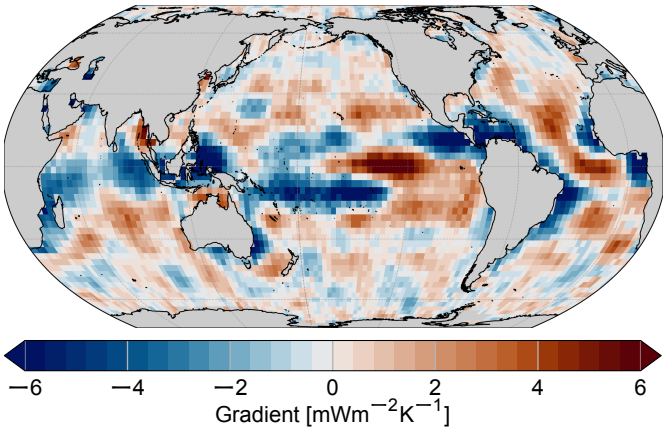

Fig. 2. **Gradient map of the convolutional neural network.** The map shows the derivative of global mean radiative response to local surface temperature, and can thus be interpreted as local radiative feedback. Gradient maps are dependent on the input, because the CNN is nonlinear. Gradients with respect to detrended temperature maps from the testing dataset are averaged.

characterizes how radiation responds to changes in temperature through processes including clouds, sea ice, or water vapor (Roe 2009; Lutsko and Takahashi 2018; Ceppi and Nowack 2021). A local positive feedback indicates that R increases when T in that location increases. This increased incoming radiation can eventually lead to higher global temperature, hence a positive feedback. Conversely, a negative feedback is stabilizing: increased temperature causes a negative response R, which slows down warming of the planet.

The gradient of the CNN (Fig. 2 and Methods) elucidates the physically meaningful regions used to make predictions. For example, the large amplitude of the gradient in the Tropics reveals that the CNN is most sensitive to temperature changes in these areas. Regions of tropical deep convection, such as the Western Pacific, show strong negative values, interpreted as negative feedbacks. These negative feedbacks are caused by changes in nonlocal lower tropospheric inversion strength, modulating low cloud coverage and hence radiation (Dong et al. 2019; Alessi and Rugenstein 2023; Wood and Bretherton 2006). In contrast, increased temperature in more stable areas (e.g., the subtropical Eastern Pacific) can cause a local decrease in shallow marine clouds and a positive radiative response, as indicated by a strong positive feedback. Importantly, the CNN learns this relationship without explicit knowledge of the underlying physical processes.

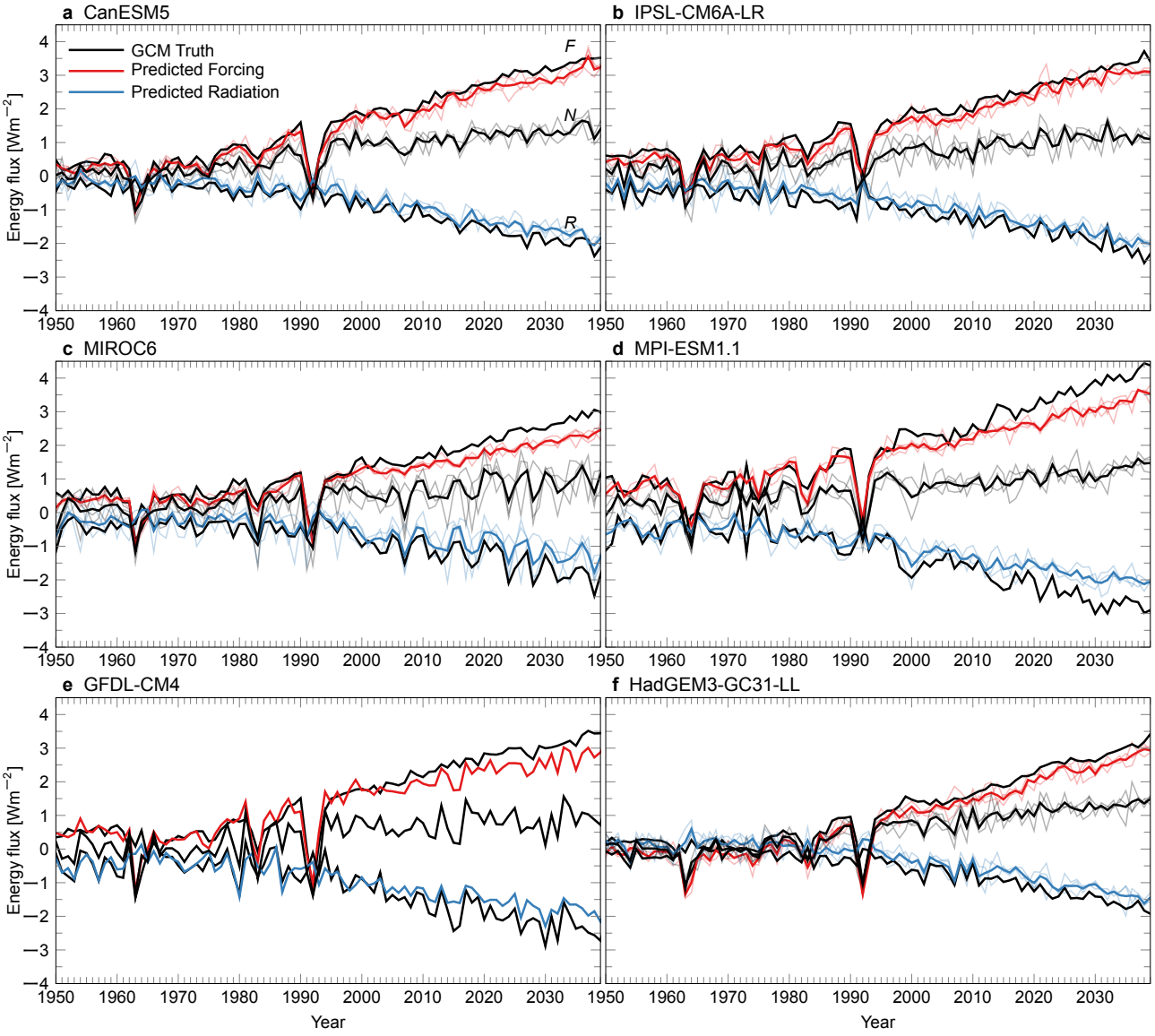

Fig. 3. **Radiative forcing estimated and simulated by six climate models.** Radiative response (R, bottom blue lines) and radiative forcing (F, top red lines) as predicted by the convolutional neural network (CNN) compared to the true model output (black lines). The middle black lines are the radiative imbalance (N) from the climate model, used to predict the forcing ($F = N - R$). Thick lines indicate ensemble averages, thin lines are individual ensemble members. The models in panel **e** and **f** were not used to train the CNN and are fully out-of-sample.

We further evaluate the reliability of our approach by using existing climate model simulations. Designated model runs can provide an estimate of F (Pincus et al. 2016, Methods), while T and N

are available as standard model output. Instead of using observations, here we use the simulated temperature maps to predict R in the climate models (Fig. 3, blue lines). Then, we subtract the simulated N (Fig. 3, middle black lines) from the result to predict F (Fig. 3, red lines). The CNN was trained on internal variability of the climate models shown in Fig. 3**a**-**d**, but the ensemble members shown were excluded from the training data. For most models, the CNN is able to reproduce the simulated F (Fig. 3, top black lines) very well for past and current values, but a systematic low bias exists for future projections. The low bias indicates that the CNN loses performance when applying warmer temperature maps than it was trained on. This suggests that also our observational estimate of the forcing might be biased low, since the internal variability seen during training is smaller than warming over the last decades. Training a CNN on forced climate change instead of internal variability removes the low bias when tested on climate models and that CNN predicts an even stronger observed trend in F in the last two decades (Supporting Information Fig. 4). However, the simulation of the forced response in climate models might be biased itself (e.g., Seager et al. 2019; Wills et al. 2022; Rugenstein et al. 2023a).

Even for internal variability, models might be biased. The CNN might not be able to extrapolate to the observed T, if all ensemble members across models used in training share a common bias. These biases in internal variability tend to vary in sign across models (e.g., Parsons et al. 2020; Maher et al. 2023). If the observed T lies within the intermodel spread of T, the CNN is expected to interpolate well to observations. To test this, we apply the CNN to the simulated temperature maps of two climate models that were not used to train the CNN (Fig. 3**e** and **f**). The CNN is able to predict R and F in these models, indicating that the CNN can generalize to new climate models. Moreover, replacing the CNN with a Green's function, a method that linearizes the response of a single atmosphere-only model to changes in the sea surface temperature (e.g., Alessi and Rugenstein 2023; Bloch-Johnson et al. 2024), leads to similar results (Supporting Information Fig. 4, Rugenstein et al. 2025). This suggests that the CNN learned a similar relationship between T and R as the Green's function, irrespective of how well the simulated internal variability represents the observed internal variability.

These tests, combined with the physically meaningful gradient maps (Fig. 2), increase our trust that our CNN learned a credible relationship between T and R and that our estimate of historical F is trustworthy. Moreover, our observation-based F is robust with respect to the choice of training

data. Training on different, fewer, or more models; training on internal variability or forced climate change; or training on pre-industrial control simulations versus detrended large ensembles does not significantly alter our results. However, we note that our uncertainty range is likely underestimated, as it only concerns the uncertainty of the 24-year regression and not the uncertainty introduced by the CNN as discussed here (see Methods).

4. Implications for past and future climate change

Our approach is independent of previous assessments of the forcing. Forster et al. (2024) (Fig. 1, top thin black line) finds a similar value based on a combination of model simulations and emission measurements. Our trend in F is somewhat higher than previous estimates (Bellouin et al. 2020; Raghuraman et al. 2021; Hodnebrog et al. 2024; Forster et al. 2024), but lies within the 5%-95% confidence range of other methods. Other estimates are restricted to shorter periods and do not include 2024 yet. Coupled climate models and atmospheric models forced with observed sea surface temperature tend to underestimate the trend in N (Olonscheck and Rugenstein 2024). This low bias translates to a low bias in the forcing estimate, if the radiative response to surface warming is taken as correct (e.g., Raghuraman et al. 2019; Hodnebrog et al. 2024). The uncertainty in our estimate of the forcing trend overlaps with these lower estimates, and the overlap depends on the evaluation period. However, because of the systematic low bias in the climate models, we argue that the forcing trend is likely higher than previously estimated.

We highlight that our method allows us to estimate F instantaneously as soon as observations of surface warming (T) and radiative imbalance (N) become available and does not rely on model intercomparison protocols, bottom-up emission estimates, or expert assessments.

a. Stabilizing feedbacks

By construction, our estimate of the forcing trend ($0.71 \pm 0.21\,\mathrm{Wm^{-2}decade^{-1}}$ for 2001-2024) is consistent with stabilizing radiative feedbacks in the last two decades. The CNN predicts a trend in R of $-0.21 \pm 0.10\,\mathrm{Wm^{-2}decade^{-1}}$. Reformulating this in terms of radiative feedbacks, i.e. $\lambda = \Delta R / \Delta \bar{T}$ with $\Delta \bar{T} = 0.22\,\mathrm{K/decade}$, we find an effective feedback parameter of $-1\,\mathrm{Wm^{-2}K^{-1}}$. Conversely, other current estimates of F imply unrealistic values of R and feedbacks. For example, using the CERES observed N ($0.51 \pm 0.17\,\mathrm{Wm^{-2}decade^{-1}}$) and estimated F by Forster et al.

(2024) ($0.52\,\mathrm{Wm^{-2}decade^{-1}}$) results in an unrealistically low $\Delta R = -0.01\,\mathrm{Wm^{-2}decade^{-1}}$, implying a feedback of only $-0.05\,\mathrm{Wm^{-2}K^{-1}}$. Using other model-based estimates of the trend in F (e.g., Hodnebrog et al. 2024) leads to a similar conclusion, because they generally agree on the trend reported by Forster et al. (2024). The latter feedback estimate suggests that increasing global temperature barely balances the excess forcing, which contradicts our understanding of feedbacks, especially the well-understood Planck feedback. This implies that the Earth's temperature would sharply increase if the feedback and forcing trend remain constant.

Our estimate of F is more realistic in terms of physical understanding of radiative feedbacks, which are universally recognized as stabilizing in the global mean for the current climate state and all commonly used future scenarios of climate change (Forster et al. 2021; Lee et al. 2021; Gregory et al. 2004, 2020; Bloch-Johnson et al. 2021; Dessler and Forster 2018a; Dessler 2010). We conclude that previous model estimates of the forcing trend are biased low or that, alternatively, the trend in N is wrong.

b. Annually resolved drivers of the radiative imbalance

Our approach gives unique insight into annual drivers of the observed radiative imbalance N. According to Eq. (1), N can be influenced by F (a particular forcing) or R (response to the observed warming patterns and radiative feedbacks). As mentioned above, the low N in 1991/1992 is consistent with a negative F from the eruption of Pinatubo (Minnis et al. 1993; Stenchikov et al. 2009), while R remained approximately constant. In contrast, in 2010, the low N occurs in conjunction with an anomalously negative R, which we attribute to high anomalous temperatures in the West Pacific and low temperatures in the East Pacific.

This annual attribution can be made more explicit by using explainable artificial intelligence (XAI). We use "input times gradient", an XAI attribution technique that calculates the local contribution of the temperature in each grid point to predict R (Shrikumar et al. 2017, see Methods). The attribution maps are calculated by multiplying detrended temperature maps with the gradient of the CNN, and thus indicate the regions that the CNN uses to make predictions. In Fig. 4**d**, we show the input times gradient map for 2010. For reference, Fig. 4**a** shows the detrended temperature anomaly in 2010. The attribution map reveals that the entire tropical Pacific contributes to the negative R in 2010, due to positive temperature anomalies in the West Pacific and negative

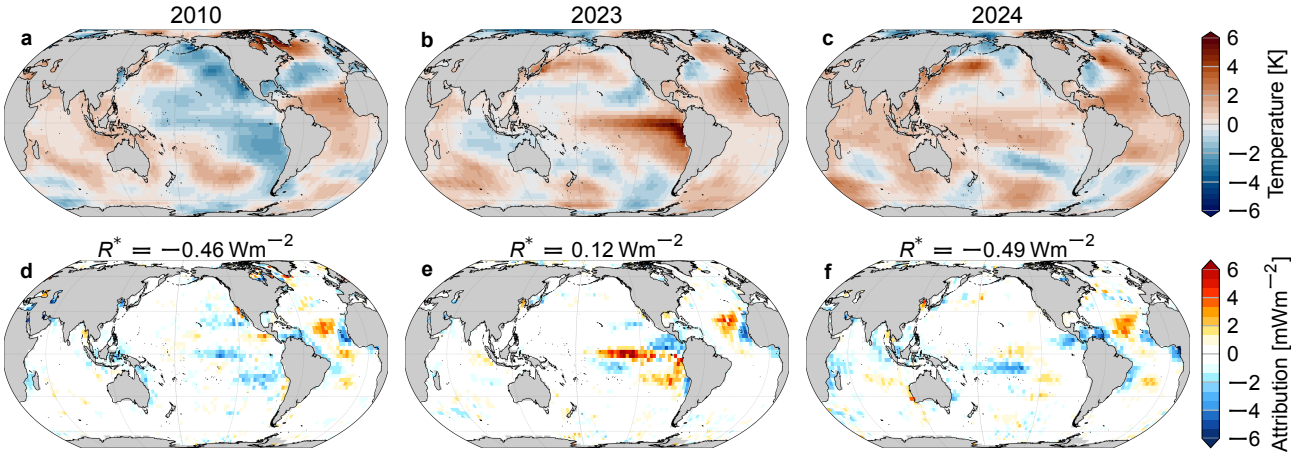

Fig. 4. **Annual attribution of the radiative response to surface warming.** Top row shows temperature anomalies from the 1995-2024 linear trend in 2010 (**a**), 2023 (**b**), and 2024 (**c**), averaged over four observational datasets. Bottom row shows the product of the temperature anomaly with the gradient of the convolutional neural network in the same year, averaged over four observational datasets, indicating the contribution of each grid point to the anomaly of global-mean radiative response to surface temperature changes. Predicted values of detrended radiation R^* for each year are given above the the attribution maps and are calculated by summing over all grid boxes.

anomalies in the East Pacific. In years with a strong El Niño event, such as 1997 and 2023, we find positive contributions to R in the equatorial East Pacific (Fig. 4**e** and Supporting Information Fig. 5; Ceppi and Fueglistaler 2021).

Since 2021, F has increased strongly (Fig. 1). One possible explanation for this increase is stricter international shipping regulations on aerosol emissions, that went into effect in 2020 (e.g., Yuan et al. 2024; Gettelman et al. 2024), although this increase in forcing might have been counter-acted by the Hunga Tonga-Hunga Ha'apai eruption in 2022 (e.g., Schoeberl et al. 2024). The rising F, in combination with a steady trend in R, contributed to an increase in the radiative imbalance from 2021 to 2023.

The year 2023 was exceptionally warm (e.g., Esper et al. 2024; Min 2024). The causes behind this record are debated, specifically in how far it was due to internal variability (e.g., Samset et al. 2024; Jiang et al. 2024; Raghuraman et al. 2024; Gyuleva et al. 2025; Xie et al. 2025) or due to external forcing (e.g., Rantanen and Laaksonen 2024; Gettelman et al. 2024; Min 2024; Kuhlbrodt et al. 2024; Schoeberl et al. 2024; Goessling et al. 2025). We find that the large N in 2023 was not

induced by a large R. In the satellite record, the observed N has never been as high, while R did not decrease enough to balance N. That is, the observed temperature pattern in 2023 did not induce a radiative effect stabilizing enough to counteract the increased F. The observed R in 2023 was largely consistent with the negative trend in R since 1995, although the El Niño pattern resulted in a positive contribution to R in the equatorial East Pacific (Fig. 4**e**). The continued increase of the forcing, together with a relatively less stabilizing radiative response, could explain the remarkably warm 2023.

In 2024, the radiative imbalance decreased significantly, which can be explained by a temperature pattern that induced a strongly negative R (Fig. 4**c** and **f**). The attribution map shows negative signals throughout the Tropics due to anomalously high temperatures.

Eq. (1) does not include the influence of natural variations on N. In principle, also the internal variability of the ocean heat content affects N, independent of F and R (Raghuraman et al. 2021). The forcing is often depicted as a fairly smooth function of time or a linear trend, such that the variability of N and R are equal (e.g., Dessler and Forster 2018b). In our case, not all of the variability of N is explained by the variability of R (Supporting Information Fig. 6). This could be because our method does not perfectly predict R from T, or because other factors, such as internal variability of ocean heat uptake unrelated to R, influence N. Due to the nature of our method, the variability of N not explained by R is assigned to F.

c. Outlook

We use the recently demonstrated dependence of global-mean radiative response to patterns of surface warming (the pattern effect) to predict effective radiative forcing with a novel framework. Our convolutional neural network allows us to rely on climate models less than traditional methods and predict physically realistic values of R. We do not rely on climate models to accurately predict a forced response to climate change, but we still use climate model data to learn the relationship between R and T from internal variability. We confirm the order of magnitude of the trend and acceleration of effective forcing, but our estimate lies on the high end of former approaches. Yet, our effective forcing estimate might still be too conservative, because tests in strong climate change scenarios indicate that the CNN underestimates the forcing (e.g., Fig. 3).

Currently, we only use the convolutional neural network to predict global values of R from observed temperature maps. Future work could break down R into its different components (e.g., shortwave or longwave) or include the spatial distribution of R to predict the spatial pattern of the effective radiative forcing. This would allow for a detailed study of local trends in F and R and could provide insight into the regional drivers of the radiative imbalance.

Our work moves towards attribution and increased physical understanding of annual values of the global-mean radiative imbalance. Combining our approach with in-situ ocean heat uptake estimates could strengthen and formalize this annual attribution. This would allow the addition of an ocean heat uptake variability term [e.g., by adding an extra term in Eq. (1)], which we leave for future development. Our framework could be used to predict radiative imbalance into the future, because surface warming and radiative forcing are, to some extent, predictable.

Materials and Methods

Convolutional neural network

The convolutional neural network (CNN) consists of a series of convolutional, max pooling, and fully connected layers (Supporting Information Fig. 1). The input data (yearly surface temperature maps) is passed through a convolutional layer with 32 kernels of size 3×3, a max pooling layer with a 2×2 kernel, a second convolutional layer (32 kernels, size 3×3), and another max pooling layer (2×2 kernel). The output from the second max pooling layer is flattened and connected to two fully connected layers, with 32 and 16 nodes, before being compared to the output (global mean radiative response to surface temperature changes, R). Every layer uses a ELU activation function, except for the last dense layer, which uses a linear one. We have tested different CNN architectures (Supporting Information Fig. 2 and Tab. 1) and chose the setup that performed best (lowest mean squared error) on the testing output data.

Because the CNN depicts a nonlinear function, its gradient is state dependent. To compute the gradient map in Fig. 2, derivatives with respect to local temperature are evaluated with the testing dataset (internal variability in the climate models, see below) and averaged over all years and ensemble members. Gradient maps averaged over members from individual climate models look similar to the one shown in Fig. 2, indicating that the average gradient in Fig. 2 is a good representation of all models. We use the CNN trained on four climate models simultaneously, under the assumption that, combined, they display enough variability to encompass observed variations of R with T.

Global climate model data

The CNN is trained on four different large ensemble climate models: CanESM5 (Swart et al. 2019), IPSL-CM6A-LR (Boucher et al. 2020), MIROC6 (Tatebe et al. 2019), and MPI-ESM1.1 (Maher et al. 2019). These models were selected based on two criteria: (1) they have at least 25 ensemble members; and (2) they contributed to the Radiative Forcing Model Intercomparison Project (RFMIP, Pincus et al. 2016), which provides dedicated simulations to quantify the radiative forcing (used as perfect model testbed in Fig. 3 and to compute the internal variability of R for training the CNN).

The input training data are maps of annual surface temperature (T). The output training data is global-mean radiative response to surface temperature changes R, computed by subtracting the forcing F from the net radiative imbalance N. We define a downward flux at the top of the atmosphere as positive. The forcing F is computed from a dedicated model run and is the same for all ensemble members, but model-dependent (Pincus et al. 2016). We average the forcing over three ensemble members provided by RFMIP, apart from MPI-ESM1.1, for which we have a single forcing time-series. N is available as standard model output as the sum of incoming shortwave, outgoing shortwave, and outgoing longwave. CanESM5, IPSL-CM6A-LR, and MIROC6 simulate the historical forcing from 1850-2014 and the Shared Socio-economic Pathway 2-4.5 (SSP2-4.5) for following years. MPI-ESM1.1 simulates historical forcing from 1871-2004 followed by the representative concentration pathway 8.5 (RCP8.5). We apply a land mask to the surface temperature, such that we can use observed sea surface temperature datasets (see below). However, using a CNN trained on surface temperature over both land and ocean does not significantly alter our results.

We use annual means from 1871 to 2039 (the longest period of overlap across the model data) and scale to the resolution of CanESM5 ($\sim 2.8°$) using a bilinear regridder with periodic boundary conditions. We use 25 ensemble members from each model, of which 19 are used for training, 3 for validation, and 3 for testing. In total, we train on $19 \times 4 = 76$ ensemble members over a period of 168 years, evenly distributed over the four models. In order to use a minimal amount of information from climate models, T and R are detrended by removing the ensemble mean (at every grid point, for each model separately), effectively removing the forcing (Suarez-Gutierrez et al. 2021). Note that detrending R and N results in the same dataset, because the forcing F is the same in every ensemble member. Hence, any climate change information is removed, except for the indirect effect of the forcing on internal variability. Only this detrended data is used to train the CNN, and thus the CNN has never seen a forced response during training.

The detrended data is representative of T- and R-anomalies with respect to the pre-industrial era, because the forced signal is removed. However, because we do not have observations in the pre-industrial era, we cannot define the observational anomalies with respect to the same pre-industrial baseline. Therefore, we redefine the training data as anomalies with respect to the 2001-2020 climatology. We do this for each model separately, by (1) calculating the average in the first twenty years of the forced simulation (1850-1871 for CanESM5, IPSL-CM6A-LR, and MIROC6; 1871-1890

for MPI-ESM1.1); (2) calculating the average in 2001-2020 of the forced simulation; (3) taking the difference between the 2001-2020 average and the pre-industrial average; and (4) subtracting this difference from the detrended training data. Each average is calculated over all ensemble members of the forced simulations of T and R. Finally, because CNNs make better predictions when the input data is centered around zero, we calculate the average across the entire training dataset (all models, all ensemble members, all years, for a given location or global mean) and subtract this average from the training data. This average is saved and used to center the testing and validation data as well. That is, when testing the CNN, anomalies are always defined with respect to the 2001-2020 climatology, but, before applying the CNN, the average of the training data is subtracted. This procedure ensures that the CNN is trained on anomalies with respect to the same climatology as the observational data.

Finally, we use data from two additional coupled climate models to test the CNN with fully out-of-sample data: GFDL-CM4 (Held et al. 2019) and HadGEM3-GC31-LL (Kuhlbrodt et al. 2018). These two models simulate the historical forcing from 1850-2014 and the SSP2-4.5 scenario from 2015-2100 and contributed to RFMIP. We use one ensemble member from GFDL-CM4 and three from HadGEM3-GC31-LL (of the 5 available). We compute yearly average temperature maps T and R, but do not detrend the data. As with the other models and observations, we use the 2001-2020 climatology to define anomalies. Importantly, these models were *not* used to train the CNN.

Observational data

When estimating the forcing (Fig. 1), we use temperature data from four different observational/reanalysis datasets: the European Centre for Medium-Range Weather Forecasts Reanalysis v5 (ERA5, Hersbach et al. 2020, 2023), COBE2 (Hirahara et al. 2014), NOAAGlobalTemp 6.0.0 (Huang et al. 2022, 2024), and The Hadley Centre Global Sea Ice and Sea Surface Temperature (HadISST-1.1, Rayner et al. 2003). All data are interpolated to the same grid as the CNN input data ($\sim 2.8°$) using a bilinear scheme with periodic boundary conditions. Note that NOAAGlobalTemp has a native grid of 5°, and thus had to be downscaled, while the other datasets have a smaller native grid. After regridding, the largest overlap of land areas across datasets is used as a land mask and applied to all training, validation, and testing data. Yearly temperature maps are defined as

anomalies with respect to the 2001-2020 climatology. The climatology is defined for each dataset separately, by averaging the temperature over 2001-2020 at each grid box.

The observational datasets (apart from ERA5) report sea surface temperature (SST), and not near-surface air temperature (TAS), on which the CNN is trained. For ERA5, we compare CNN predictions based on SST and TAS and find similar values of R (Supporting Information Fig. 4**a**, TAS is used in the main text). The forcing trend predicted from SST is slightly lower than the one predicted from TAS, but is not significantly different (Supporting Information Fig. 7**b**).

For the observed radiative imbalance N, we use satellite observations from CERES-EBAF4.2.1 (Loeb et al. 2018; NASA/LARC/SD/ASDC 2023). Yearly averages from 2001-2024 are computed from monthly data of globally-averaged net top of the atmosphere radiative fluxes. From 1985-2000, we use a reconstruction (DEEP-C, Allan et al. 2014; Liu et al. 2020) based on older satellite observations and model simulations. Note that the reconstruction before 2001 uses models and reanalyses, and is therefore less reliable than the direct observations derived from CERES (Raghuraman et al. 2019, 2023; Loeb et al. 2024a). We use anomalies of N with respect to the 2001-2020 climatology of CERES.

Trend analysis

Trends are calculated from yearly averages using ordinary least squares. We include predictions from all four temperature datasets in the calculation of the overall trend. We compare the overall trend with the trend of individual observational datasets and find similar results (within 5-95% confidence bounds). For the individual datasets, we find a trend in F of $0.70 \pm 0.21\,\mathrm{Wm^{-2}decade^{-1}}$ (ERA5), $0.69 \pm 0.21\,\mathrm{Wm^{-2}decade^{-1}}$ (COBE2), $0.75 \pm 0.20\,\mathrm{Wm^{-2}decade^{-1}}$ (NOAAGlobalTemp), and $0.69 \pm 0.20\,\mathrm{Wm^{-2}decade^{-1}}$ (HadISST-1.1). The spread across different datasets could be because there are differences in surface temperature trends across these datasets, which can be large, even in the satellite era (e.g., Menemenlis et al. 2025). However, because the trends in F are very similar, differences between sea surface temperature datasets seem to have a small effect on the trend in F.

We estimate the uncertainty in the trend of F by combining the uncertainties in the trends in N and R. Raghuraman et al. (2021) estimated the 95% confidence range of the trend in N to be $0.20\,\mathrm{Wm^{-2}decade^{-1}}$, which encompasses different observational uncertainties (see also Loeb

et al. 2021, 2022; Hodnebrog et al. 2024). Assuming a normal distribution, this converts to a standard error of $\sigma_N = 0.10\,\mathrm{Wm^{-2}decade^{-1}}$. The standard error of the trend in R is computed for every observational dataset separately, and the mean is taken over all four datasets, that is, $\sigma_R^2 = \sum_{j=1}^{5} \sigma_j^2/5$. The uncertainty in the trend in R does not include any uncertainty introduced by the CNN. Finally, the standard error of the trend in F is estimated to be $\sigma_F = \sqrt{\sigma_N^2 + \sigma_R^2}$, and converted to a 5-95% confidence range by assuming the trend slope follows a t-distribution with 21 degrees of freedom.

We compare our estimate of the trend in F to data from Forster et al. (2024). We use the 100 000-member probabilistic Monte Carlo ensemble of their effective radiative forcing estimate and calculate the trend in 2001-2023 for each ensemble member. The mean over all 100 000 trends is $0.52\,\mathrm{Wm^{-2}decade^{-1}}$, with a 5-95% confidence range of $0.36\,\mathrm{Wm^{-2}decade^{-1}}$ to $0.68\,\mathrm{Wm^{-2}decade^{-1}}$. Our mean estimate of $0.72\,\mathrm{Wm^{-2}decade^{-1}}$ in 2001-2023 coincides with the 97.5% percentile of the probabilistic ensemble.

Annual attribution

To attribute the regions that mostly contribute to the prediction of R, we make use of "input times gradient", an explainable artificial intelligence (XAI) technique that attributes the output of the CNN to the input features (Shrikumar et al. 2017; Mamalakis et al. 2022). Because we are interested in the interannual variability of the prediction, we apply the method to detrended data.

First, we compute the gradient of the CNN with respect to the observed temperature map in each year y and denote it as $\nabla_T R(y)$. Note that the gradient depends on the year, because the CNN is nonlinear. Second, for each grid box, we calculate the trend in the observed temperature from 1995 to 2024 using ordinary least squares regression, $\hat{T}(y) = ay + b$. Finally, in a given year y, we multiply the detrended temperature with the gradient to find the attribution map $\rho(y) = [T(y) - \hat{T}(y)] \times \nabla_T R(y)$. We follow this procedure for all four observational datasets separately, and average over the four results to obtain the final attribution maps.

In a given year, the sum of all grid boxes j in the attribution map is approximately equal to the detrended radiative response, $R^*(y) = \sum_j \rho_j(y) \approx R(y) - \hat{R}(y)$, with $\hat{R}$ being the trend in R from 1995-2024. This is an approximation because the input times gradient technique approximates the

nonlinear CNN with a linear function. More advanced XAI techniques for attribution maps that exactly sum up to the predicted value lead to similar results.

Data availability

All climate model data is standard CMIP model output, and is made freely available by the Earth System Grid Federation (ESGF) at https://esgf-node.llnl.gov/. The effective radiative forcing timeseries from Forster et al. (2024) can be downloaded from https://github.com/ClimateIndicator/forcing-timeseries/releases/tag/v6.2.1. Observational temperature data is available from https://doi.org/10.24381/cds.adbb2d47 (ERA5), https://psl.noaa.gov/data/gridded/data.cobe2.html (COBE2), https://www.ncei.noaa.gov/products/land-based-station/noaa-global-temp (NOAAGlobalTemp), and https://www.metoffice.gov.uk/hadobs/hadisst/ (HadISST-1.1). The observed radiative imbalance can be downloaded at https://ceres.larc.nasa.gov/data/ (CERES-EBAF4.2.1) and https://researchdata.reading.ac.uk/347/ (DEEP-C).

Code availability

All reported results were analyzed using Python-3.10, and the CNNs were trained using Tensorflow-2.15. All code will be made available at the time of acceptance of the manuscript.

Acknowledgements

We thank Dirk Olonscheck for sharing large-ensemble and forcing climate model data and Mark Zelinka for sharing observational temperature datasets. We thank Marybeth Arcodia, Candace Bethea, Leif Fredericks, Rich Karp, and Shiv Priyam Raghuraman for comments on the manuscript. This work was supported, in part, by the Regional and Global Model Analysis program area of the U.S. Department of Energy's (DOE) Office of Biological and Environmental Research (BER) as part of the Program for Coordinated Model Diagnosis and Intercomparison (PCMDI). Maria Rugenstein was funded by NASA under 80NSSC21K1042.

Supporting Information

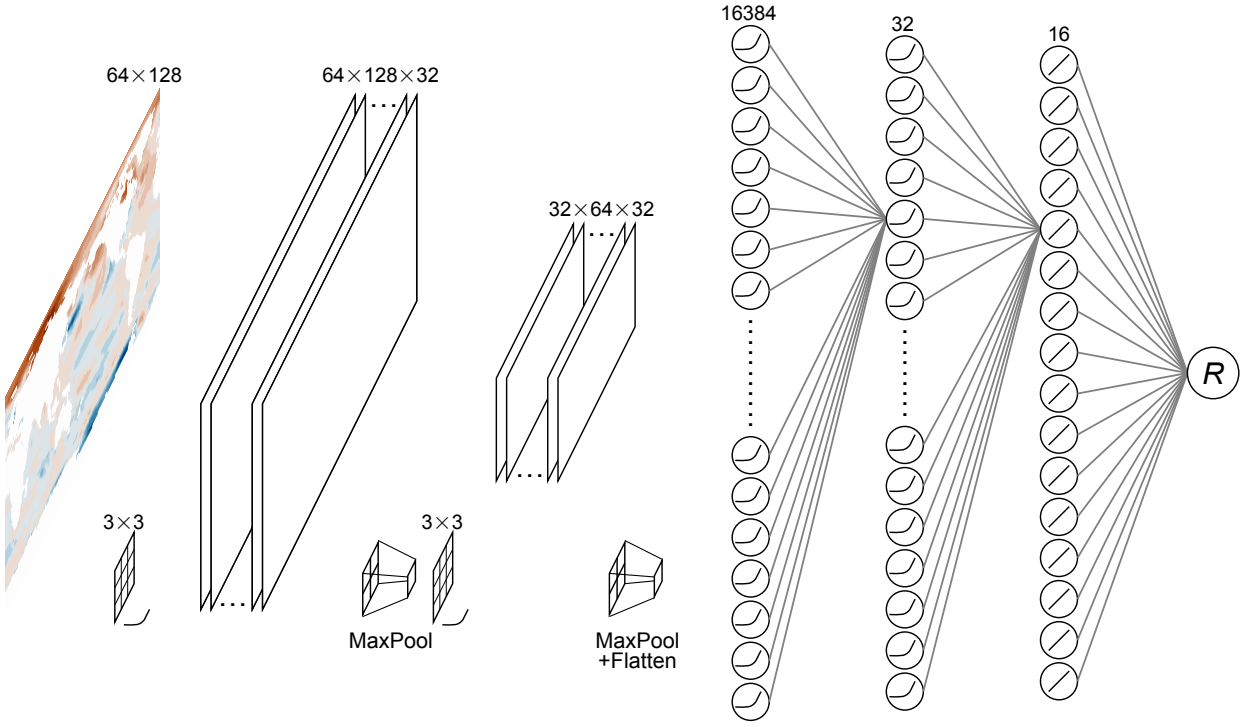

Supporting Information Fig. 1. **Schematic of the architecture of the CNN used.** The input maps (surface temperature) are passed through two convolutional layers, each with 32 kernels of size 3×3 and followed by a max pooling layer and an ELU activation function. The result is flattened and passed through two additional fully connected layers with 32 and 16 neurons, with a ELU and linear activation function respectively. The final result is a single number estimating the global-mean radiative response R.

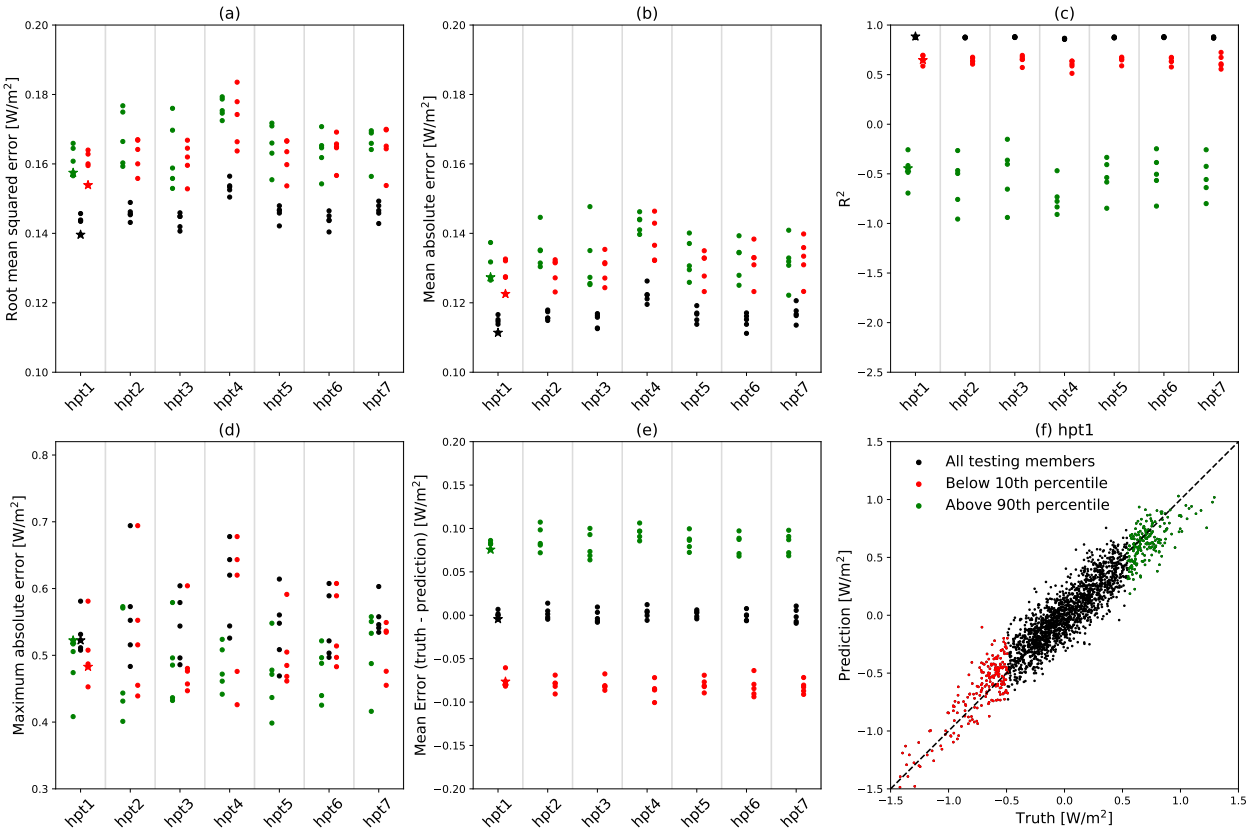

Supporting Information Fig. 2. **Hyperparameter testing for different CNN architectures.** The x-axis labels are defined in Supporting Information Tab. 1, and each dot represents a different random initialization of the CNN before training. For each trained CNN, we compute the (a) root mean squared error, (b) mean absolute error, (c) R^2 value, (d) maximum absolute error , and (e) mean error (truth−prediction). Panel (f) reports the truth versus prediction of all years in the testing dataset. Black dots represent all years, while red and green dots show only those in the lower and upper 10th percentiles, to examine how well the CNN performs on the extremes. The CNN used in the main text is highlighted by a star.

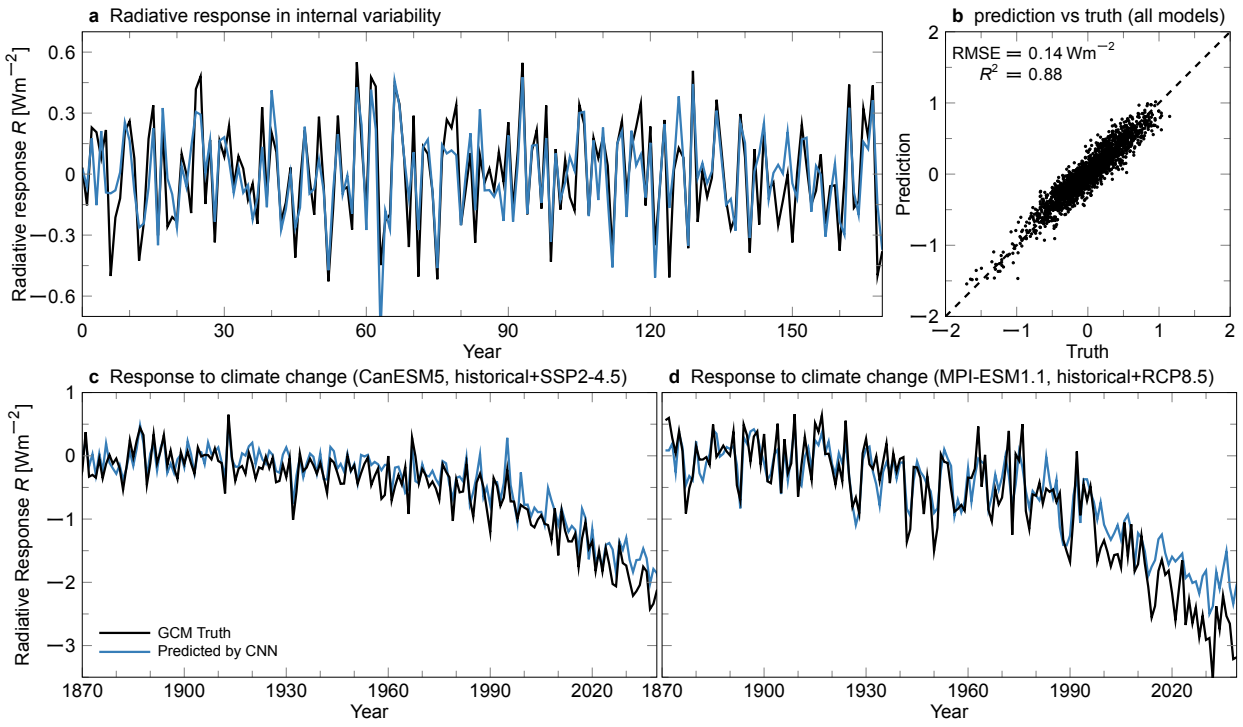

525 **Supporting Information Fig.** 3. **Verification of the CNN.** Panel (a) shows the truth (black) and predictions
526 (blue) for a single ensemble member in the testing dataset, for internal variability of the temperature and radiative
527 response. Panel (b) shows the true versus the predicted radiative response for all years in the testing dataset; the
528 CNN explains 85 % of the variance across all testing members. Panels (c) and (d) show the CNN applied to an
529 out-of-sample member that experiences forced climate change for two different models used in training. Even
530 though the CNN has never seen climate change during training, it can predict the response to forcing well.

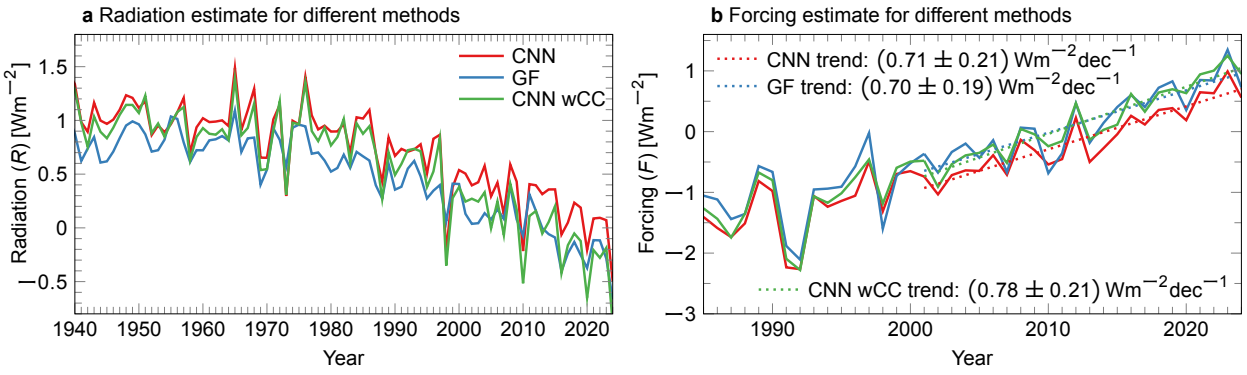

Supporting Information Fig. 4. **Comparison of the convolutional neural network versus a Green's function approach**. Panel (a) shows the predicted radiative response (R) and (b) shows the predicted forcing ($F = N - R$). Dotted lines in (b) are forcing trends in 2001-2024. We show the predictions averaged over four different observational datasets (see Methods). Red lines are predictions from the convolutional neural network trained on internal variability (CNN, as in the main text), green lines are predictions from a convolutional neural network trained on forced climate change (CNN wCC), and blue lines are predictions made by convolving the observational temperature maps with the Green's function (GF) of ECHAM6 (Alessi and Rugenstein 2023). The Green's function is a method that captures the causal response of a single atmospheric model to changes in the sea surface temperature (Bloch-Johnson et al. 2024). Because the Green's function method uses atmosphere-only simulations, it does not rely on the simulated warming patterns from a coupled model. However, the method forces the atmospheric model with artificial surface temperature perturbations, and thus does not sample the system in its natural state (see Rugenstein et al. 2025, for an in-depth comparison of the CNN to the Green's function method). Note that the Green's function of Alessi and Rugenstein (2023) is tuned to obtain the correct magnitude of the radiative response in a future RCP8.5 scenario.

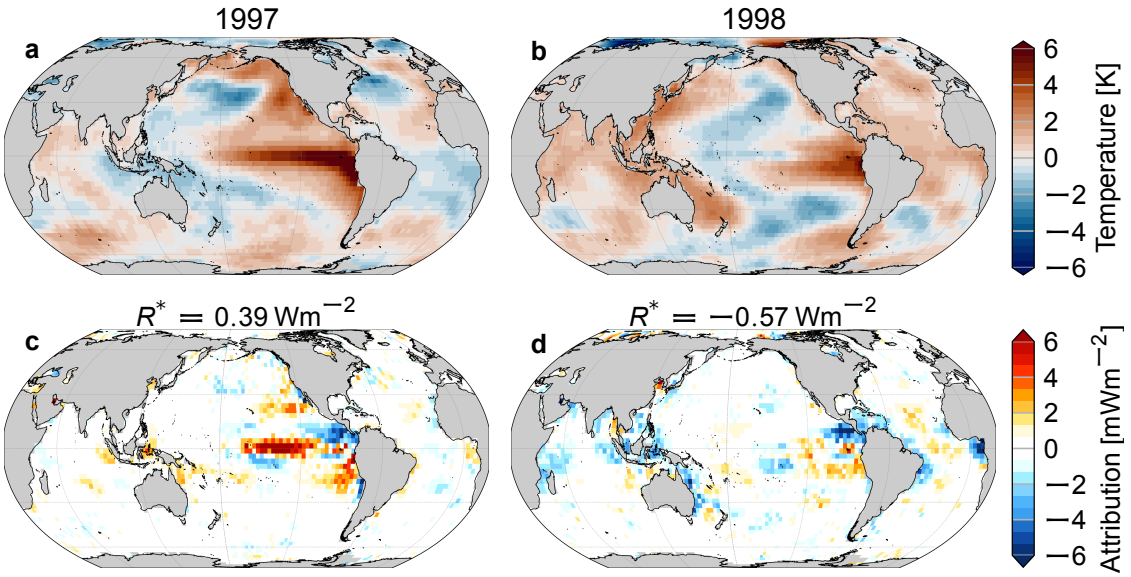

Supporting Information Fig. 5. **Annual attribution of the radiative response to surface warming.** Top row shows linearly detrended temperature anomalies in 1997 (a) and 1998 (a), averaged over four observational datasets. Bottom row shows the product of the temperature anomaly with the gradient of the convolutional neural network in the same year, averaged over four observational datasets, indicating the contribution of each grid point to the anomaly of global-mean radiative response to surface temperature changes. Predicted values of detrended radiation R^* for each year are given above the the attribution maps and are calculated by summing over all grid boxes.

Supporting Information Table 1. **Hyperparameters used in testing different CNN architectures in Supporting Information Fig. 2.** All CNNs use a similar architecture as shown in Supporting Information Fig. 1, but we change the number of convolutional layers/kernels, kernel size, and amount of dense layers/nodes. The set of hyperparameters used in the main text is hpt1.

	Convolutional layers	Kernel size	Dense layers
hpt1	[32, 32]	3×3	[32, 16]
hpt2	[32, 32]	5×5	[32, 16]
hpt3	[64, 64]	3×3	[32, 16]
hpt4	[32, 32, 32]	3×3	[32, 16]
hpt5	[16, 16]	3×3	[32, 16]
hpt6	[32, 32]	3×3	[16, 16]
hpt7	[32, 32]	3×3	[8, 8, 16]

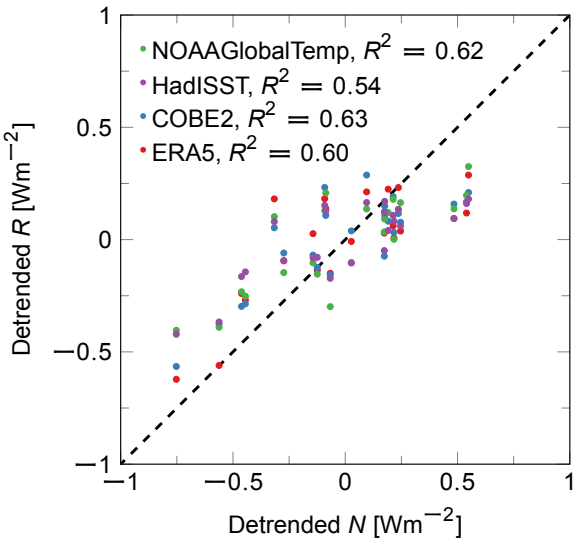

552 **Supporting Information Fig.** 6. **Variability of radiative response versus radiative imbalance**. The linearly
553 detrended yearly global-mean values of R predicted by the CNN for the four observational datasets versus linearly
554 detrended N from CERES. If the variability of R and N around the trend is the same, all data points should lie
555 on the 1:1 line (dashed black). The correlation coefficient is given in the legend.

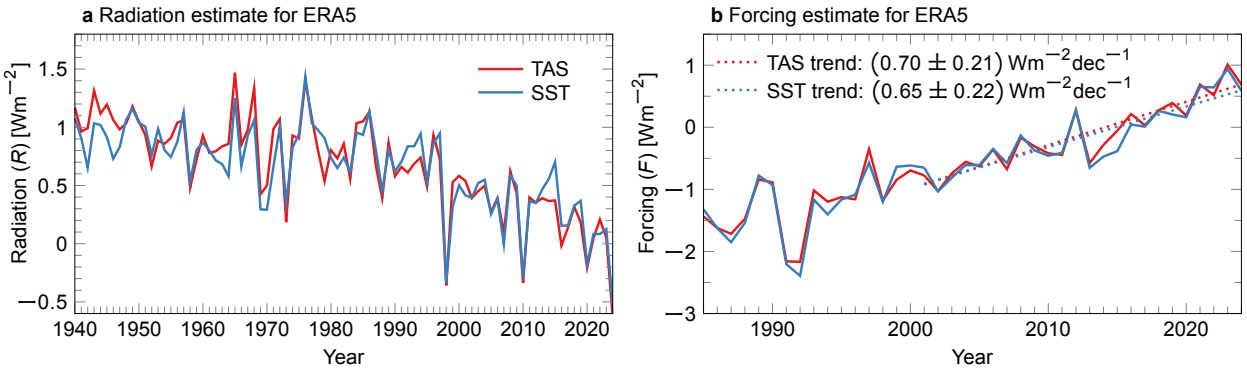

556 **Supporting Information Fig.** 7. **Comparison of near-surface temperature (TAS) and sea surface temper-**
557 **ature (SST) as input for the convolutional neural network**. Panel (a) shows the predicted radiative response
558 (R) and (b) shows the predicted forcing ($F = N - R$). Dotted lines in (b) are forcing trends in 2001-2024. We use
559 ERA5 data and our CNN from the main text. Both predictions are very similar; therefore, we expect only minor
560 differences when using observational datasets of SST compared to TAS.

References

Alessi, M. J., and M. Rugenstein, 2023: Surface Temperature Pattern Scenarios Suggest Higher Warming Rates Than Current Projections. *Geophysical Research Letters*, **50 (23)**, e2023GL105 795, https://doi.org/10.1029/2023GL105795.

Allan, R. P., C. Liu, N. G. Loeb, M. D. Palmer, M. Roberts, D. Smith, and P.-L. Vidale, 2014: Changes in global net radiative imbalance 1985–2012. *Geophysical research letters*, **41 (15)**, 5588–5597, https://doi.org/10.1002/2014GL060962.

Andrews, T., and P. M. Forster, 2020: Energy budget constraints on historical radiative forcing. *Nature Climate Change*, **10 (4)**, 313–316, https://doi.org/10.1038/s41558-020-0696-1.

Andrews, T., J. M. Gregory, and M. J. Webb, 2015: The Dependence of Radiative Forcing and Feedback on Evolving Patterns of Surface Temperature Change in Climate Models. *Journal of Climate*, **28 (4)**, 1630–1648, https://doi.org/10.1175/JCLI-D-14-00545.1.

Bellouin, N., and Coauthors, 2020: Bounding Global Aerosol Radiative Forcing of Climate Change. *Reviews of Geophysics*, **58 (1)**, e2019RG000 660, https://doi.org/10.1029/2019RG000660.

Bloch-Johnson, J., M. Rugenstein, M. B. Stolpe, T. Rohrschneider, Y. Zheng, and J. M. Gregory, 2021: Climate Sensitivity Increases Under Higher CO2 Levels Due to Feedback Temperature Dependence. *Geophysical Research Letters*, **48 (4)**, e2020GL089 074, https://doi.org/10.1029/2020GL089074.

Bloch-Johnson, J., and Coauthors, 2024: The Green's Function Model Intercomparison Project (GFMIP) Protocol. *Journal of Advances in Modeling Earth Systems*, **16 (2)**, e2023MS003 700, https://doi.org/https://doi.org/10.1029/2023MS003700.

Boucher, O., and Coauthors, 2020: Presentation and evaluation of the IPSL-CM6A-LR climate model. *Journal of Advances in Modeling Earth Systems*, **12 (7)**, e2019MS002 010, https://doi.org/10.1029/2019MS002010.

Ceppi, P., and S. Fueglistaler, 2021: The El Niño-Southern Oscillation Pattern Effect. *Geophysical Research Letters*, **48 (21)**, e2021GL095 261, https://doi.org/10.1029/2021GL095261.

Ceppi, P., and P. Nowack, 2021: Observational evidence that cloud feedback amplifies global warming. *Proceedings of the National Academy of Sciences*, **118 (30)**, https://doi.org/10.1073/pnas.2026290118.

Cess, R. D., and Coauthors, 1990: Intercomparison and interpretation of climate feedback processes in 19 atmospheric general circulation models. *Journal of Geophysical Research: Atmospheres*, **95 (D10)**, 16 601–16 615, https://doi.org/10.1029/JD095iD10p16601.

Charney, J., and Coauthors, 1979: Carbon Dioxide and Climate: A Scientific Assessment. Tech. rep., National Academy of Science, Washington, DC. https://doi.org/10.17226/12181.

Cheng, L., K. Von Schuckmann, A. Minière, M. Z. Hakuba, S. Purkey, G. A. Schmidt, and Y. Pan, 2024: Ocean heat content in 2023. *Nature Reviews Earth & Environment*, **5 (4)**, 232–234, https://doi.org/10.1038/s43017-024-00539-9.

Dessler, A. E., 2010: A Determination of the Cloud Feedback from Climate Variations over the Past Decade. *Science*, **330 (6010)**, 1523–1527, https://doi.org/10.1126/science.1192546.

Dessler, A. E., and P. M. Forster, 2018a: An Estimate of Equilibrium Climate Sensitivity From Interannual Variability. *Journal of Geophysical Research: Atmospheres*, **123 (16)**, 8634–8645, https://doi.org/10.1029/2018JD028481.

Dessler, A. E., and P. M. Forster, 2018b: An Estimate of Equilibrium Climate Sensitivity From Interannual Variability. *Journal of Geophysical Research: Atmospheres*, **123 (16)**, 8634–8645, https://doi.org/10.1029/2018JD028481.

Dong, Y., C. Proistosescu, K. C. Armour, and D. S. Battisti, 2019: Attributing Historical and Future Evolution of Radiative Feedbacks to Regional Warming Patterns using a Green's Function Approach: The Preeminence of the Western Pacific. *Journal of Climate*, **32 (17)**, 5471–5491, https://doi.org/10.1175/JCLI-D-18-0843.1.

Esper, J., M. Torbenson, and U. Büntgen, 2024: 2023 summer warmth unparalleled over the past 2,000 years. *Nature*, **631 (8019)**, 94–97, https://doi.org/10.1038/s41586-024-07512-y.

Forster, P., and Coauthors, 2021: The Earth's Energy Budget, Climate Feedbacks, and Climate Sensitivity. *Climate Change 2021: The Physical Science Basis. Contribution of Working Group I to the Sixth Assessment Report of the Intergovernmental Panel on Climate Change*, V. Masson-Delmotte, P. Zhai, A. Pirani, S. L. Connors, C. Péan, S. Berger, N. Caud, Y. Chen, L. Goldfarb, M. I. Gomis, M. Huang, K. Leitzell, E. Lonnoy, J. B. R. Matthews, T. K. Maycock, T. Waterfield, O. Yelekçi, R. Yu, and B. Zhou, Eds., Cambridge University Press, Cambridge, UK and New York, NY, USA, book section 7, 923–1054, https://doi.org/10.1017/9781009157896.009.

Forster, P. M., and Coauthors, 2024: Indicators of Global Climate Change 2023: annual update of key indicators of the state of the climate system and human influence. *Earth System Science Data*, **16 (6)**, 2625–2658, https://doi.org/10.5194/essd-16-2625-2024.

Gettelman, A., and Coauthors, 2024: Has Reducing Ship Emissions Brought Forward Global Warming? *Geophysical Research Letters*, **51 (15)**, e2024GL109 077, https://doi.org/10.1029/2024GL109077.

Goessling, H. F., T. Rackow, and T. Jung, 2025: Recent global temperature surge intensified by record-low planetary albedo. *Science*, **387 (6729)**, 68–73, https://doi.org/10.1126/science.adq7280.

Gregory, J. M., T. Andrews, P. Ceppi, T. Mauritsen, and M. J. Webb, 2020: How accurately can the climate sensitivity to CO2 be estimated from historical climate change? *Climate Dynamics*, **54 (1)**, 129–157, https://doi.org/10.1007/s00382-019-04991-y.

Gregory, J. M., and Coauthors, 2004: A new method for diagnosing radiative forcing and climate sensitivity. *Geophysical Research Letters*, **31 (3)**, https://doi.org/10.1029/2003GL018747.

Gyuleva, G., R. Knutti, and S. Sippel, 2025: Combination of Internal Variability and Forced Response Reconciles Observed 2023-2024 Warming. *Authorea Preprints*, https://doi.org/10.22541/essoar.173869655.55297060/v1.

Held, I. M., and Coauthors, 2019: Structure and Performance of GFDL's CM4.0 Climate Model. *Journal of Advances in Modeling Earth Systems*, **11 (11)**, 3691–3727, https://doi.org/10.1029/2019MS001829.

Hersbach, H., and Coauthors, 2020: The ERA5 global reanalysis. *Quarterly Journal of the Royal Meteorological Society*, **146 (730)**, 1999–2049, https://doi.org/10.1002/qj.3803.

Hersbach, H., and Coauthors, 2023: ERA5 hourly data on single levels from 1940 to present. Copernicus Climate Change Service (C3S) Climate Data Store (CDS). https://doi.org/10.24381/cds.adbb2d47.

Hirahara, S., M. Ishii, and Y. Fukuda, 2014: Centennial-Scale Sea Surface Temperature Analysis and Its Uncertainty. *Journal of Climate*, **27 (1)**, 57 – 75, https://doi.org/10.1175/JCLI-D-12-00837.1.

Hodnebrog, Ø., and Coauthors, 2024: Recent reductions in aerosol emissions have increased Earth's energy imbalance. *Communications Earth & Environment*, **5 (1)**, 166, https://doi.org/10.1038/s43247-024-01324-8.

Huang, B., X. Yin, M. J. Menne, R. Vose, and H.-M. Zhang, 2022: Improvements to the Land Surface Air Temperature Reconstruction in NOAAGlobalTemp: An Artificial Neural Network Approach. *Artificial Intelligence for the Earth Systems*, **1 (4)**, e220 032, https://doi.org/10.1175/AIES-D-22-0032.1.

Huang, B., X. Yin, M. J. Menne, R. S. Vose, and H.-M. Zhang, 2024: NOAA Global Surface Temperature Dataset (NOAAGlobalTemp), Version 6.0.0. https://doi.org/10.25921/rzxg-p717.

Jiang, N., and Coauthors, 2024: Enhanced risk of record-breaking regional temperatures during the 2023–24 El Niño. *Scientific Reports*, **14 (1)**, 2521, https://doi.org/10.1038/s41598-024-52846-2.

Johnson, G. C., J. M. Lyman, and N. G. Loeb, 2016: Improving estimates of Earth's energy imbalance. *Nature Climate Change*, **6 (7)**, 639–640, https://doi.org/10.1038/nclimate3043.

Knutti, R., and M. A. A. Rugenstein, 2015: Feedbacks, climate sensitivity and the limits of linear models. *Philosophical Transactions of the Royal Society of London A: Mathematical, Physical and Engineering Sciences*, **373 (2054)**, https://doi.org/10.1098/rsta.2015.0146.

Kramer, R. J., H. He, B. J. Soden, L. Oreopoulos, G. Myhre, P. M. Forster, and C. J. Smith, 2021: Observational Evidence of Increasing Global Radiative Forcing. *Geophysical Research Letters*, **48 (7)**, e2020GL091 585, https://doi.org/10.1029/2020GL091585.

Kuhlbrodt, T., R. Swaminathan, P. Ceppi, and T. Wilder, 2024: A Glimpse into the Future: The 2023 Ocean Temperature and Sea Ice Extremes in the Context of Longer-Term Climate Change. *Bulletin of the American Meteorological Society*, **105 (3)**, E474 – E485, https://doi.org/10.1175/BAMS-D-23-0209.1.

Kuhlbrodt, T., and Coauthors, 2018: The Low-Resolution Version of HadGEM3 GC3.1: Development and Evaluation for Global Climate. *Journal of Advances in Modeling Earth Systems*, **10 (11)**, 2865–2888, https://doi.org/10.1029/2018MS001370.

LeCun, Y., Y. Bengio, and G. Hinton, 2015: Deep learning. *Nature*, **521 (7553)**, 436–444, https://doi.org/10.1038/nature14539.

Lee, J.-Y., and Coauthors, 2021: Future Global Climate: Scenario-Based Projections and Near-Term Information. *Climate Change 2021: The Physical Science Basis. Contribution of Working Group I to the Sixth Assessment Report of the Intergovernmental Panel on Climate Change*, V. Masson-Delmotte, P. Zhai, A. Pirani, S. L. Connors, C. Péan, S. Berger, N. Caud, Y. Chen, L. Goldfarb, M. I. Gomis, M. Huang, K. Leitzell, E. Lonnoy, J. B. R. Matthews, T. K. Maycock, T. Waterfield, O. Yelekçi, R. Yu, and B. Zhou, Eds., Cambridge University Press, Cambridge,

UK and New York, NY, USA, book section 4, 553–672, https://doi.org/10.1017/9781009157896.006.

Liu, C., and R. Allan, 2022: Reconstructions of the radiation fluxes at the top of atmosphere and net surface energy flux: DEEP-C Version 5.0. University of Reading, URL https://researchdata.reading.ac.uk/347/, https://doi.org/10.1175/JCLI-D-17-0137.1.

Liu, C., and Coauthors, 2020: Variability in the global energy budget and transports 1985–2017. *Climate Dynamics*, **55**, 3381–3396, https://doi.org/10.1007/s00382-020-05451-8.

Loeb, N. G., D. R. Doelling, S. Kato, W. Su, P. E. Mlynczak, and J. C. Wilkins, 2024a: Continuity in Top-of-Atmosphere Earth Radiation Budget Observations. *Journal of Climate*, https://doi.org/10.1175/JCLI-D-24-0180.1.

Loeb, N. G., S.-H. Ham, R. P. Allan, T. J. Thorsen, B. Meyssignac, S. Kato, G. C. Johnson, and J. M. Lyman, 2024b: Observational Assessment of Changes in Earth's Energy Imbalance Since 2000. *Surveys in Geophysics*, https://doi.org/10.1007/s10712-024-09838-8.

Loeb, N. G., G. C. Johnson, T. J. Thorsen, J. M. Lyman, F. G. Rose, and S. Kato, 2021: Satellite and Ocean Data Reveal Marked Increase in Earth's Heating Rate. *Geophysical Research Letters*, e2021GL093047, https://doi.org/10.1029/2021GL093047.

Loeb, N. G., and Coauthors, 2018: Clouds and the Earth's Radiant Energy System (CERES) Energy Balanced and Filled (EBAF) Top-of-Atmosphere (TOA) Edition-4.0 Data Product. *Journal of Climate*, **31 (2)**, 895 – 918, https://doi.org/10.1175/JCLI-D-17-0208.1.

Loeb, N. G., and Coauthors, 2022: Evaluating twenty-year trends in Earth's energy flows from observations and reanalyses. *Journal of Geophysical Research: Atmospheres*, **127 (12)**, e2022JD036 686, https://doi.org/10.1029/2022JD036686.

Lutsko, N. J., and K. Takahashi, 2018: What Can the Internal Variability of CMIP5 Models Tell Us about Their Climate Sensitivity? *Journal of Climate*, **31 (13)**, 5051–5069, https://doi.org/10.1175/JCLI-D-17-0736.1.

Maher, N., and Coauthors, 2019: The Max Planck Institute Grand Ensemble: Enabling the Exploration of Climate System Variability. *Journal of Advances in Modeling Earth Systems*, **11 (7)**, 2050–2069, https://doi.org/10.1029/2019MS001639.

Maher, N., and Coauthors, 2023: The future of the El Niño–Southern Oscillation: using large ensembles to illuminate time-varying responses and inter-model differences. *Earth System Dynamics*, **14 (2)**, 413–431, https://doi.org/10.5194/esd-14-413-2023.

Mamalakis, A., E. A. Barnes, and I. Ebert-Uphoff, 2022: Investigating the Fidelity of Explainable Artificial Intelligence Methods for Applications of Convolutional Neural Networks in Geoscience. *Artificial Intelligence for the Earth Systems*, **1 (4)**, e220 012, https://doi.org/10.1175/AIES-D-22-0012.1.

Menemenlis, S., G. Vecchi, W. Yang, S. Fueglistaler, and S. P. Raghuraman, 2025: Consequential Differences in Satellite-Era Sea Surface Temperature Trends Across Datasets. *Research Square*, https://doi.org/10.21203/rs.3.rs-5493841/v1.

Min, S.-K., 2024: Human influence can explain the widespread exceptional warmth in 2023. *Communications Earth & Environment*, **5 (1)**, 215, https://doi.org/10.1038/s43247-024-01391-x.

Minnis, P., E. F. Harrison, L. L. Stowe, G. Gibson, F. M. Denn, D. Doelling, and W. Smith Jr, 1993: Radiative climate forcing by the Mount Pinatubo eruption. *Science*, **259 (5100)**, 1411–1415, https://doi.org/10.1126/science.259.5100.1411.

Myers, T. A., R. C. Scott, M. D. Zelinka, S. A. Klein, J. R. Norris, and P. M. Caldwell, 2021: Observational constraints on low cloud feedback reduce uncertainty of climate sensitivity. *Nature Climate Change*, **11 (6)**, 501–507, https://doi.org/10.1038/s41558-021-01039-0.

NASA/LARC/SD/ASDC, 2023: CERES Energy Balanced and Filled (EBAF) TOA and Surface Monthly means data in netCDF Edition 4.2. NASA Langley Atmospheric Science Data Center DAAC, https://doi.org/10.5067/TERRA-AQUA-NOAA20/CERES/EBAF_L3B004.2.

Olonscheck, D., and M. Rugenstein, 2024: Coupled Climate Models Systematically Underestimate Radiation Response to Surface Warming. *Geophysical Research Letters*, **51 (6)**, e2023GL106 909, https://doi.org/10.1029/2023GL106909.

Parsons, L. A., M. K. Brennan, R. C. Wills, and C. Proistosescu, 2020: Magnitudes and Spatial Patterns of Interdecadal Temperature Variability in CMIP6. *Geophysical Research Letters*, **47 (7)**, e2019GL086 588, https://doi.org/10.1029/2019GL086588.

Pincus, R., P. M. Forster, and B. Stevens, 2016: The Radiative Forcing Model Intercomparison Project (RFMIP): experimental protocol for CMIP6. *Geoscientific Model Development*, **9 (9)**, 3447–3460, https://doi.org/10.5194/gmd-9-3447-2016.

Quaas, J., and Coauthors, 2022: Robust evidence for reversal of the trend in aerosol effective climate forcing. *Atmospheric Chemistry and Physics*, **22 (18)**, 12 221–12 239, https://doi.org/10.5194/acp-22-12221-2022.

Raghuraman, S. P., D. Paynter, R. Menzel, and V. Ramaswamy, 2023: Forcing, Cloud Feedbacks, Cloud Masking, and Internal Variability in the Cloud Radiative Effect Satellite Record. *Journal of Climate*, **36 (12)**, 4151 – 4167, https://doi.org/10.1175/JCLI-D-22-0555.1.

Raghuraman, S. P., D. Paynter, and V. Ramaswamy, 2019: Quantifying the Drivers of the Clear Sky Greenhouse Effect, 2000-2016. *Journal of Geophysical Research: Atmospheres*, **124 (21)**, 11 354–11 371, https://doi.org/10.1029/2019JD031017.

Raghuraman, S. P., D. Paynter, and V. Ramaswamy, 2021: Anthropogenic forcing and response yield observed positive trend in Earth's energy imbalance. *Nature Communications*, **12 (1)**, 4577, https://doi.org/10.1038/s41467-021-24544-4.

Raghuraman, S. P., B. Soden, A. Clement, G. Vecchi, S. Menemenlis, and W. Yang, 2024: The 2023 global warming spike was driven by the El Niño–Southern Oscillation. *Atmospheric Chemistry and Physics*, **24 (19)**, 11 275–11 283, https://doi.org/10.5194/acp-24-11275-2024.

Rantanen, M., and A. Laaksonen, 2024: The jump in global temperatures in September 2023 is extremely unlikely due to internal climate variability alone. *npj Climate and Atmospheric Science*, **7 (1)**, 34, https://doi.org/10.1038/s41612-024-00582-9.

Rayner, N. A., D. E. Parker, E. B. Horton, C. K. Folland, L. V. Alexander, D. P. Rowell, E. C. Kent, and A. Kaplan, 2003: Global analyses of sea surface temperature, sea ice, and night marine air temperature since the late nineteenth century. *Journal of Geophysical Research: Atmospheres*, **108 (D14)**, https://doi.org/10.1029/2002JD002670.

Reichstein, M., G. Camps-Valls, B. Stevens, M. Jung, J. Denzler, N. Carvalhais, and Prabhat, 2019: Deep learning and process understanding for data-driven Earth system science. *Nature*, **566 (7743)**, 195–204, https://doi.org/10.1038/s41586-019-0912-1.

Roe, G., 2009: Feedbacks, Timescales, and Seeing Red. *Annual Review of Earth and Planetary Sciences*, **37 (1)**, 93–115, https://doi.org/10.1146/annurev.earth.061008.134734.

Rugenstein, M., S. Dhame, D. Olonscheck, R. C. J. Wills, M. Watanabe, and R. Seager, 2023a: Connecting the SST Pattern Problem and the Hot Model Problem. *Geophysical Research Letters*, **50 (22)**, e2023GL105 488, https://doi.org/10.1029/2023GL105488.

Rugenstein, M., S. Van Loon, and E. A. Barnes, 2025: Convolutional Neural Networks Trained on Internal Variability Predict Forced Response of TOA Radiation by Learning the Pattern Effect. *Geophysical Research Letters*, **52 (4)**, e2024GL109 581, https://doi.org/10.1029/2024GL109581.

Rugenstein, M., M. Zelinka, K. B. Karnauskas, P. Ceppi, and T. Andrews, 2023b: Patterns of Surface Warming Matter for Climate Sensitivity. *Eos*, **104**, https://doi.org/10.1029/2023EO230411.

Samset, B. H., M. T. Lund, J. S. Fuglestvedt, and L. J. Wilcox, 2024: 2023 temperatures reflect steady global warming and internal sea surface temperature variability. *Communications Earth & Environment*, **5 (1)**, 460, https://doi.org/10.1038/s43247-024-01637-8.

Schoeberl, M. R., Y. Wang, G. Taha, D. J. Zawada, R. Ueyama, and A. Dessler, 2024: Evolution of the Climate Forcing During the Two Years after the Hunga Tonga-Hunga Ha'apai Eruption. *ESS Open Archive*, https://doi.org/10.22541/essoar.171255733.32358374/v1.

Seager, R., M. Cane, N. Henderson, D.-E. Lee, R. Abernathey, and H. Zhang, 2019: Strengthening tropical Pacific zonal sea surface temperature gradient consistent with rising greenhouse gases. *Nature Climate Change*, **9 (7)**, 517–522, https://doi.org/10.1038/s41558-019-0505-x.

Senior, C. A., and J. F. B. Mitchell, 2000: The time-dependence of climate sensitivity. *Geophysical Research Letters*, **27 (17)**, 2685–2688, https://doi.org/10.1029/2000GL011373.

Sherwood, S. C., S. Bony, O. Boucher, C. Bretherton, P. M. Forster, J. M. Gregory, and B. Stevens, 2015: Adjustments in the Forcing-Feedback Framework for Understanding Climate Change. *Bulletin of the American Meteorological Society*, **96 (2)**, 217 – 228, https://doi.org/10.1175/BAMS-D-13-00167.1.

Sherwood, S. C., and Coauthors, 2020: An Assessment of Earth's Climate Sensitivity Using Multiple Lines of Evidence. *Reviews of Geophysics*, **58 (4)**, https://doi.org/10.1029/2019RG000678.

Shrikumar, A., P. Greenside, and A. Kundaje, 2017: Learning Important Features Through Propagating Activation Differences. *Proceedings of the 34th International Conference on Machine Learning*, D. Precup, and Y. W. Teh, Eds., PMLR, Proceedings of Machine Learning Research, Vol. 70, 3145–3153.

Smith, C. J., and Coauthors, 2020: Effective radiative forcing and adjustments in CMIP6 models. *Atmospheric Chemistry and Physics*, **20 (16)**, 9591–9618, https://doi.org/10.5194/acp-20-9591-2020.

Soden, B. J., W. D. Collins, and D. R. Feldman, 2018: Reducing uncertainties in climate models. *Science*, **361 (6400)**, 326–327, https://doi.org/10.1126/science.aau1864.

Stenchikov, G., T. L. Delworth, V. Ramaswamy, R. J. Stouffer, A. Wittenberg, and F. Zeng, 2009: Volcanic signals in oceans. *Journal of Geophysical Research: Atmospheres*, **114 (D16)**, https://doi.org/10.1029/2008JD011673.

Storto, A., and C. Yang, 2024: Acceleration of the ocean warming from 1961 to 2022 unveiled by large-ensemble reanalyses. *Nature Communications*, **15 (1)**, 545, https://doi.org/10.1038/s41467-024-44749-7.

Suarez-Gutierrez, L., S. Milinski, and N. Maher, 2021: Exploiting large ensembles for a better yet simpler climate model evaluation. *Climate Dynamics*, **57 (9)**, 2557–2580, https://doi.org/10.1007/s00382-021-05821-w.

Swart, N. C., and Coauthors, 2019: The Canadian earth system model version 5 (CanESM5. 0.3). *Geoscientific Model Development*, **12 (11)**, 4823–4873, https://doi.org/10.5194/gmd-12-4823-2019.

Tatebe, H., and Coauthors, 2019: Description and basic evaluation of simulated mean state, internal variability, and climate sensitivity in MIROC6. *Geoscientific Model Development*, **12 (7)**, 2727–2765, https://doi.org/10.5194/gmd-12-2727-2019.

von Schuckmann, K., and Coauthors, 2023: Heat stored in the Earth system 1960–2020: where does the energy go? *Earth System Science Data*, **15 (4)**, 1675–1709, https://doi.org/10.5194/essd-15-1675-2023.

Wills, R. C. J., Y. Dong, C. Proistosecu, K. C. Armour, and D. S. Battisti, 2022: Systematic Climate Model Biases in the Large-Scale Patterns of Recent Sea-Surface Temperature and Sea-Level Pressure Change. *Geophysical Research Letters*, **49 (17)**, e2022GL100 011, https://doi.org/10.1029/2022GL100011.

Wood, R., and C. S. Bretherton, 2006: On the Relationship between Stratiform Low Cloud Cover and Lower-Tropospheric Stability. *Journal of Climate*, **19 (24)**, 6425 – 6432, https://doi.org/10.1175/JCLI3988.1.

Xie, S.-P., A. Miyamoto, P. Zhang, Y. Kosaka, Y. Liang, and N. J. Lutsko, 2025: What made 2023 and 2024 the hottest years in a row? *npj Climate and Atmospheric Science*, **8 (1)**, 117, https://doi.org/10.1038/s41612-025-01006-y.

Yuan, T., and Coauthors, 2024: Abrupt reduction in shipping emission as an inadvertent geoengineering termination shock produces substantial radiative warming. *Communications Earth & Environment*, **5 (1)**, 281, https://doi.org/10.1038/s43247-024-01442-3.